Materials Today Bio 29 (2024) 101357

Contents lists available at ScienceDirect

Materials Today Bio

journal homepage: www.journals.elsevier.com/materials-today-bio

5-Hydroxytryptophan artificial synaptic vesicles across the blood-brain barrier for the rapid-acting treatment of depressive disorder

Peng Chang [a], Jingwen Ma [b], Ke Li [c], Wei Wang [d], Dan Chen [a], Zhe Liu [e], Wenhua Zhan [d,**], Yun Zeng [a,***], Yonghua Zhan [a,*]

[a] School of Life Science and Technology, Xidian University and Engineering Research Center of Molecular and Neuro Imaging, Ministry of Education, Xi'an, 710126, PR China
[b] Medical Imaging Center, Ninth Hospital of Xi'an, Xi'an, 710054, PR China
[c] Xi'an Key Laboratory for Prevention and Treatment of Common Aging Diseases, Translational and Research Centre for Prevention and Therapy of Chronic Disease, Institute of Basic and Translational Medicine, Xi'an Medical University, Xi'an, 710021, PR China
[d] Department of Radiation Oncology, General Hospital of Ningxia Medical University, Yinchuan, 750004, PR China
[e] Department of Pathology, Ninth Hospital of Xi'an, Xi'an, 710054, PR China

ARTICLE INFO

Keywords:
Depression
5-HTP
Vesicles
Blood-brain barrier
Photothermal-triggered

ABSTRACT

Conventional antidepressants are slow to work and have serious side effects and poor response rates. As a precursor to 5-hydroxytryptamine (5-HT), 5-hydroxytryptophan (5-HTP) can be safely increased in concentration and rapidly metabolized into 5-HT in the brain, but the effectiveness of 5-HTP is severely limited due to its short half-life and lack of targeting. To traverse the blood-brain barrier (BBB) and achieve effective targeting, we designed a near-infrared (NIR) light-responsive artificial synaptic vesicles functionalized with an aptamer and loaded with 5-HTP and IR780. Photothermal approaches could improve the BBB permeability, and photothermal-triggered 5-HTP release could also be achieved. The ability to penetrate the BBB and enhance cerebral drug enrichment could be observed by fluorescence imaging. In addition, the nanoplatform incorporating the NIR laser considerably reduced depressive-like behaviors in chronic unpredictable moderate stress model mice in only 4 weeks, suggesting a potential approach for rapid-acting depression treatment.

1. Introduction

Depression is a prevalent, expensive, and incapacitating condition that has been associated with an elevated risk of suicide, and it is now one of the primary global public health concerns [1,2]. The selective serotonin reuptake inhibitor (SSRI) class of antidepressants, which include fluvoxamine, paroxetine, and fluoxetine, *etc.*, are the most often prescribed antidepressant medications [3,4]. Their primary action is to inhibit 5-hydroxytryptamine (5-HT) reuptake by selectively acting on the serotonergic system and the presynaptic membrane, thus increasing the concentration of intersynaptic 5-HT to achieve antidepressant effects [5,6]. Although these medications are effective, the oral dose is difficult to regulate and lacks specificity, often requiring 6 weeks or more to take effect. In addition, they might induce adverse side effects such as serotonin syndrome, gastrointestinal issues, allergies, agitation/restlessness, and sexual dysfunction [7]. Traditional antidepressant medications also have poor reactivity. Clinical studies have shown that approximately 30 % of depressed individuals do not respond to these medications [8–11]. Hence, it is essential to expedite the development of innovative pharmaceuticals for depression treatment. 5-hydroxytryptophan (5-HTP) may safely increase intracranial 5-HT concentrations by being rapidly metabolized into 5-HT once it enters the brain. However, due to its lack of targeting and short half-life (< 2 h), 5-HTP is not effective in clinical antidepressant treatment. Therefore, the enhancement of bioavailability has emerged as a crucial factor in determining the potential therapeutic use of 5-HTP. By addressing its pharmacokinetic restrictions, 5-HTP might be made into an effective therapeutic antidepressant medicine by controlled release, which would increase its pharmacological efficacy [12,13]. Additionally, antidepressant medication toxicity and therapeutic efficacy may be also mitigated *via* nanocarrier-based delivery

* Corresponding author.
** Corresponding author.
*** Corresponding author.
E-mail addresses: zhanwhgood@163.com (W. Zhan), yzeng@xidian.edu.cn (Y. Zeng), yhzhan@xidian.edu.cn (Y. Zhan).

https://doi.org/10.1016/j.mtbio.2024.101357
Received 24 September 2024; Received in revised form 12 November 2024; Accepted 21 November 2024
Available online 22 November 2024
2590-0064/© 2024 The Authors. Published by Elsevier Ltd. This is an open access article under the CC BY-NC license (http://creativecommons.org/licenses/by-nc/4.0/).

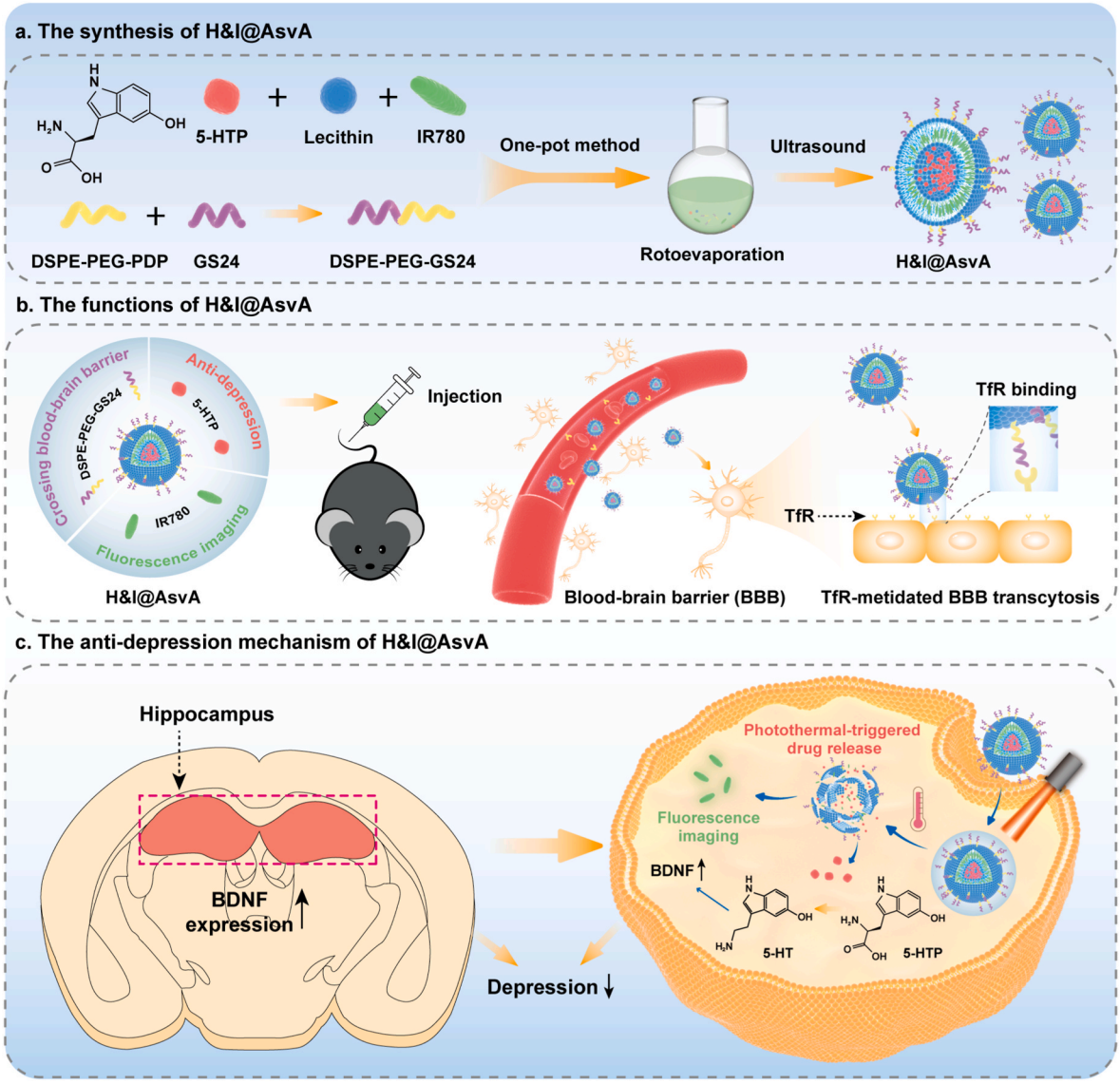

Fig. 1. Schematic illustration of H&I@AsvA synthesis and its antidepressant mechanism. a) Synthesis of H&I@AsvA. b) The functions of H&I@AsvA. c) The antidepressant mechanism of H&I@AsvA.

methods [14]. However, there are currently no effective nanocarriers available for 5-HTP administration to maximize antidepressant benefits. Therefore, to shorten the onset time, it is essential to explore more reasonable and efficient strategies for delivering 5-HTP.

Assuring efficient drug accumulation in the brain for successful antidepressant treatment is one of the most significant goals [15]. However, it is difficult for nanocarriers to transfer drugs to the brain because the blood-brain barrier (BBB) acts as a "wall" between blood flow and brain cells [16–19]. Because of their high BBB penetration and excellent biocompatibility, vesicles have great potential as a drug delivery system for the treatment of brain-related diseases [19–22]. To activate acetylcholinesterase, Quan et al. created aptamer-modified liposomes loaded with an acetylcholinesterase reactivator. This liposome can successfully penetrate the BBB [23]. Nevertheless, to achieve rapid-acting treatments for depression, nanocarriers must be able to cross the BBB and guarantee that the drugs contained within can be rapidly released into the brain. Photothermal-triggered release, as a noninvasive physical means, provides a potential strategy for controlled drug release to the brain [14, 24]. Wang et al. created a near-infrared (NIR) light-responsive black-phosphorus nanosheet loaded with fluoxetine. NIR-induced photothermal effects allowed the nanosheets to cross the BBB and achieve rapid fluoxetine release [14]. Furthermore, our earlier research has shown that photothermal effects may not only increase BBB permeability and boost the efficacy of nanocarriers across the BBB but also induce the rupture of nanocarriers to facilitate rapid drug release [25]. Nevertheless, most photothermal-triggered research is currently focused on glioma therapy, and inspired by the reuptake of intersynaptic vesicles, artificial synaptic vesicles (Asv) have gained significant interest from researchers in treating central nervous system diseases [26,27], but no investigation was reported regarding the treatment of depressive disorder. Therefore, developing a photothermal-triggered drug release Asv may achieve brain accumulation and rapid release of 5-HTP, providing an effective rapid-acting treatment strategy for depression.

Here, we present an aptamer-functionalized NIR light-responsive Asv. The synthesis route, functions, and antidepressant mechanisms of 5-HTP & IR780@Asv-Apt (H&I@AsvA) are shown in Fig. 1. A straightforward and effective one-pot approach is available for the synthesis of H&I@AsvA. With the aptamer, H&I@AsvA can cross the BBB more precisely and efficiently. Using an *in vitro* BBB model and *in vivo* fluorescence imaging, we validated the targeting capability of H&I@AsvA. Moreover, laser irradiation might quickly heat H&I@AsvA, increasing the BBB permeability and accelerating the rupture of Asv to release 5-

HTP. Notably, the combination of intravenous H&I@AsvA and NIR laser irradiation successfully shortened the onset of antidepressant effects, drastically improving depression symptoms within 4 weeks. In summary, this work provides a novel approach to brain drug administration and a novel strategy to achieve rapid-acting treatment for depression.

2. Materials and methods

2.1. Synthesis of H&I@AsvA

50 μL of DNA aptamers (GS24, 5.0 nmol, as shown in Table S1) were mixed with 10 μL tris (2-carboxyethyl) phosphine (TCEP) solution (5.0 nmol, 0.05 mol L^{-1}) for 1 h. To produce DSPE-PEG-Apt, the DNA aptamers were purified using a G-25 column (Nap-5 Columns Sephadex G-25 DNA Grade) and then co-incubated with three times the molar amount of a DSPE-PEG-PDP solution (30 μL) in the absence of light for a duration of 24 h. The UV–Vis spectrophotometer was used to measure the peak at 343 nm.

The filming-rehydration ultrasonic dispersion process was used to produce Asv. Then, 15 mg of 5-HTP was dissolved in 30 mL of anhydrous ethanol to obtain a 0.5 mg mL^{-1} 5-HTP solution, and the above 5-HTP solution, 40 mg of lecithin, 5 mg of cholesterol, 500 μg of IR780, 0.1 mg of vitamin E (for antioxidant use), and DSPE-PEG-Apt were dissolved in 40 mL of trichloromethane in a 200 mL round flask, which was immersed in an ultrasonic cleaner at 100 W for 2 min and then placed in a rotary evaporator at 40 °C and 80 rpm for 40 min under reduced pressure. 10 mL of di-water was added, and the mixture was thoroughly hydrated using an ultrasonic cleaner. Once the membrane layer on the wall of the flask was hydrated and evenly distributed, the flask was subjected to ultrasonic cell disruption at a power of 140 W for 30 min in an ice bath. Subsequently, the flask was centrifuged at 10 000×*g* for 10 min to obtain H&I@AsvA in the supernatant.

2.2. Characterizations of H&I@AsvA

Transmission electron microscopy (TEM) was used to examine the morphology of H&I@AsvA. The Malvern dynamic light scattering (DLS) particle size analyzer was used to evaluate the hydrated particle size of Asv and H&I@AsvA, as well as the surface Zeta potential of Asv, 5-HTP@Asv (H@Asv), 5-HTP & IR780@Asv (H&I@Asv), and H&I@AsvA. The UV–Vis–NIR spectra of 5-HTP, IR780, H@Asv, H&I@Asv, and H&I@AsvA were analyzed using a UV–Vis–NIR spectrophotometer to determine their distinctive peaks. The assessment of *in vitro* stability included the measurement of the hydrated particle size of H&I@AsvA in PBS at 4 and 37 °C over a period of 7 days or in 10 % fetal bovine serum (FBS) at 4 °C over a period of 7 h.

2.3. Release of 5-HTP from H&I@AsvA

To establish the standard curve of 5-HTP, a 1.0 mg mL^{-1} solution of 5-HTP was prepared and then diluted to concentrations of 0.01, 0.02, 0.03, 0.04, and 0.05 mg mL^{-1} using DMSO. The absorbance at 276 nm was then measured using a UV–Vis spectrophotometer. The drug encapsulation efficiency (DEE) and drug loading content (DLC) were determined by dialysis. Equations S1 and S2 were used to determine the DEE and DLC of H&I@AsvA. The dialysis method was used to determine the *in vitro* release of free 5-HTP, H@Asv, H&I@AsvA, and H&I@AsvA after 808 nm laser irradiation. The dialysis bag was supplemented with 500 μL of each sample solution, while the external solution consisted of 10 mL of di-water. The mixture was then incubated at 37 °C. To estimate the cumulative release curves, the concentration of 5-HTP in the external solution was determined using a UV–Vis spectrophotometer at time intervals of 0.5, 1, 3, 6, 12, 24, and 48 h.

2.4. Photothermal conversion performance of H&I@AsvA

The evaluation of *in vitro* photothermal performance was conducted by introducing 1.0 mL of the sample into a 1.5 mL centrifuge tube. The fiber-optic collimator was positioned vertically, approximately 1.0 cm above the centrifuge tube. The photothermal performance of several materials was examined by the application of a 2.0 W cm^{-2} laser to PBS, H@AsvA, and H&I@AsvA. The temperature was then measured for 5 min at 30 s-intervals using an NIR thermographic camera. The approaches were used to evaluate the photothermal characteristics of the nanoplatforms under various laser powers (0.5, 1.0, 1.5, and 2.0 W cm^{-2}) and various concentrations of H&I@AsvA (IR780 concentrations: 3.75, 7.50, 15.0, and 30.0 μg mL^{-1}). In addition, H&I@AsvA underwent continuous heating using an 808 nm laser, with a temperature increase of 5 min followed by a cooling period of 5 min in each cycle. The photothermal conversion efficiency (PCE) of H&I@AsvA was assessed by measuring the temperature difference between the ascending and descending phases over 6 cycles. Equation S3 was used for calculating the PCE. The evaluation of *in vivo* photothermal performance included the administration of 200 μL of PBS, H&I@Asv, or H&I@AsvA to C57BL/6J mice. Twenty-four hours after the injection, the brain regions of the mice were exposed to an 808 nm laser at a power of 2.0 W cm^{-2} for 5 min. The NIR thermographic camera was used to measure fluctuations in the body temperature of mice before and after irradiation.

2.5. In vitro fluorescence imaging of H&I@AsvA

The IVIS small animal imaging system was used to evaluate the fluorescence imaging capability of H&I@AsvA. Fluorescence imaging was conducted by placing 1.0 mL of various concentrations of H&I@AsvA (IR780 concentrations: 0.1875, 0.375, 0.750, 1.500, and 3.000 μg mL^{-1}) in a 1.5 mL centrifuge tube. The excitation wavelength (Ex) used in this experiment was 780 nm, whereas the emission wavelength (Em) employed was 845 nm.

2.6. In vitro cell culture studies

2.6.1. In vitro cell viability

The RSC-96 cells, bEnd.3 cells (BBB endothelial cells), and HUVECs were cultivated in DMEM supplemented with 10 % FBS and thereafter placed in an incubator set at 37 °C and 5 % CO_2. Once the cells had adhered to the 96-well plate and reached an estimated growth rate of 80 %, the medium was substituted with a new mixture containing varying concentrations of DOX (0.037, 0.111, 0.333, 1.000 μg mL^{-1}) and H&I@AsvA (5-HTP concentrations: 3.0, 9.0, 27, and 81 μg mL^{-1}). The cells were placed in a CO_2 incubator for 24 h, after which 10 μL of CCK-8 solution was added to each well to maintain the incubation process for an additional 2 h. The cytotoxicity of H&I@AsvA to RSC-96 cells, bEnd.3 cells, and HUVECs was assessed by measuring the absorbance of each well at 450 nm and calculating the cell viability using a microplate reader.

2.6.2. Cell uptake

In the study of cell uptake using confocal laser scanning microscopy (CLSM), IR780 was replaced with IR676 (Ex/Em: 620/670 nm) in H&I@AsvA. After reaching a growth rate of approximately 70 %, the bEnd.3 cells were removed from the previous medium and rinsed three times with PBS. Subsequently, 1.0 mL of serum-free medium containing H&I@AsvA was added, and the cells were cultured for durations of 1, 2, 4, 6, 8, and 12 h. The medium was removed, and the cells were subjected to three washes with PBS, followed by fixation with 4 % paraformaldehyde. Subsequently, the cells were washed three times with PBS. Next, 100 μL of DAPI was added to stain the nuclei. The cells were then rinsed three times with PBS. The CLSM was used to monitor the uptake of H&I@AsvA. DAPI emitted blue fluorescence (Ex/Em: 405/430–470 nm), while IR676 emitted red fluorescence (Ex/Em: 620/670

nm). ImageJ was used to quantify the fluorescence intensity of the cell uptake.

2.6.3. In vitro BBB model

In the *in vitro* BBB model, bEnd.3 cells were grown for 72 h on gelatin-coated Transwell plates with a pore size of 0.4 μm until they reached confluence. The measurement of aptamer transcytosis was conducted from the basal chamber using the IVIS imaging system at 12 h after the attainment of a trans-endothelial electrical resistance of 100 Ω cm^2 in the model. H@Asv, H&I@Asv, H&I@AsvN (Non-targeting sequence DNA with the same number of bases as GS24), and H&I@AsvA were added to the apical side of the Transwell plate.

2.7. In vivo fluorescence imaging of H&I@AsvA

All animal experiments were performed in accordance with the animal ethics of the affiliated institutions (No. 2022-058). The mice were administered 50 μL of PBS, H&I@Asv, or H&I@AsvA (IR780 concentration: 50 μg mL^{-1}) *via* the tail vein for fluorescence imaging. The IVIS imaging system was used to acquire fluorescence images at different time intervals (0, 1, 2, 4, 8, 12, 24, 48, and 72 h) after injection. Then, the mice were euthanized, and the heart, liver, spleen, lung, kidney, and brain tissues were removed for fluorescence imaging. The Ex/Em wavelengths used were 780 and 845 nm. The quantitative analysis of fluorescence intensity was conducted using Living Image (version 4.3.1).

2.8. Hemolysis and acute toxicity tests

The hemolysis test used 4 % sheep blood erythrocytes, with 1 % Triton X-100 solution serving as the positive control and PBS serving as the negative control. A total of 20 μL of each sample, including 1 % Triton X-100, saline, Asv, H@Asv, H&I@Asv, and H&I@AsvA, together with 480 μL of saline and 500 μL of a 4 % sheep blood erythrocyte suspension, was added to a 1.5 mL centrifuge tube. The tubes were then placed at 37 °C for 2 h. Following the incubation period, the tubes were centrifuged at a force of 10 000×*g* for 5 min. Subsequently, 200 μL of the supernatant from each group was carefully and slowly transferred onto a 96-well plate, and measured using a microplate reader. The absorbance at a wavelength of 545 nm was then recorded. The calculation of hemolysis rates for various samples was performed using the following equation:

$$\text{Hemolysis rate}\ (\%) = \frac{OD_S - OD_N}{OD_P - OD_N} \times 100\%$$

OD_N indicates the absorbance at 545 nm of PBS, OD_P indicates the absorbance at 545 nm after treatment with 1 % Triton X-100, and OD_S indicates the absorbance at 545 nm after treatment with different samples.

Fifteen BALB/c mice (18–20 g, approximately 8 weeks old) were randomly divided into 5 groups: saline, 5-HTP, Asv, H&I@AsvA, and H&I@AsvA with 808 nm laser irradiation (H&I@AsvA-NIR), and all the solutions were injected through the tail vein. Mice were kept surviving for 14 days, at which point their survival rates and body weights were determined. Then, the mice were euthanized, and heart, liver, spleen, lung, kidney, and brain tissues were fixed in 4 % paraformaldehyde and stored at 4 °C for further sectioning, staining, and analysis. Moreover, liver, renal function, and cardiac enzyme tests were conducted using biochemical analysis.

2.9. Construction of chronic unpredictable mild stress (CUMS) mouse model

C57BL/6J mice (male, 15–17 g, approximately 4 weeks old) were subjected to CUMS to establish an animal model of depression according to previously reported methods [14]. According to the data shown in Table S2, the stressors used in the study were forced swimming, centrifugal tube restraint, cage rotation, water and food fasting, day and night reversal, and cold isolation. To prevent mice from habituating stressors, one of the stressors was randomly administered daily at various intervals. Prior to the behavioral test, the CUMS process was conducted for 50 days. The mice in the control group were relocated from their cages to the experimental room, where they were handled with care for 2–4 min. They were then returned to the feeding room approximately 2 h later.

2.10. Mouse behavioral tests

The depression-like behaviors of the mice were assessed using the sucrose preference test (SPT), forced swim test (FST), and tail suspension test (TST) [14]. To guarantee the dependability of the data, the vicinity was devoid of any noise or other environmental variables during the examinations.

2.10.1. SPT

The mice were individually caged 3 days before the test day. The mice were trained to adapt to a 1 % sucrose solution for 4 days as follows: during day 1 and 2, both tubes were filled with normal drinking water, during day 3 and 4, both tubes were filled with 1 % sucrose solution. The SPT was performed between day 5 and 8, with both tubes being filled with 1 % sucrose solution (tube A) and normal drinking water (tube B). During the test, the mice could freely feed on the solutions in tubes A and B, and the two tubes were switched daily to avoid side deflection. The consumed solution from each tube was measured and the sucrose preference was calculated using the following equation:

$$\text{Sucrose preference}(\%) = \frac{V_A}{V_A + V_B} \times 100\%$$

where V_A and V_B refer to the liquids consumed in tubes A and B, respectively.

2.10.2. FST

The mice were placed individually in a 2000 mL beaker (25 cm in height and 19 cm in diameter). The beaker was filled with water (15 cm in height) and maintained at 25 °C. The duration of the FST was 6 min, during which it was captured using a video camera. To mitigate any potential impact on subsequent mice, the di-water was replaced after each experimental trial. The duration of immobility was recorded during the last 4 min by an investigator who was blinded to the treatment. The mice were considered immobile since they maintained floating and exhibited little movement other than keeping their noses above the water.

2.10.3. TST

Each mouse was hung separately by affixing its tail to a vertical pole, with the head positioned approximately 30 cm away from the table. The duration of the TST was 6 min, during which it was captured using a video camera. The duration of immobility was recorded during the last 4 min by an investigator who was blinded to the treatment. The mice were considered motionless when they were passively hung and maintained immobility in their limbs.

2.11. In vivo antidepressant treatment behavioral tests

The experimental mice were divided into 6 groups (n = 6): a) non-stress mice serving as the control group, b) saline, c) 5-HTP, d) H&I@Asv, e) H&I@AsvA, and f) H&I@AsvA-NIR. In the 5-HTP group, 5-HTP was administered intraperitoneally, whereas in the other groups, the nanoplatform was administered *via* the tail vein. The medication was administered at 4-day intervals for a duration of 4 weeks. After a two-week treatment period, behavioral assessments were conducted for

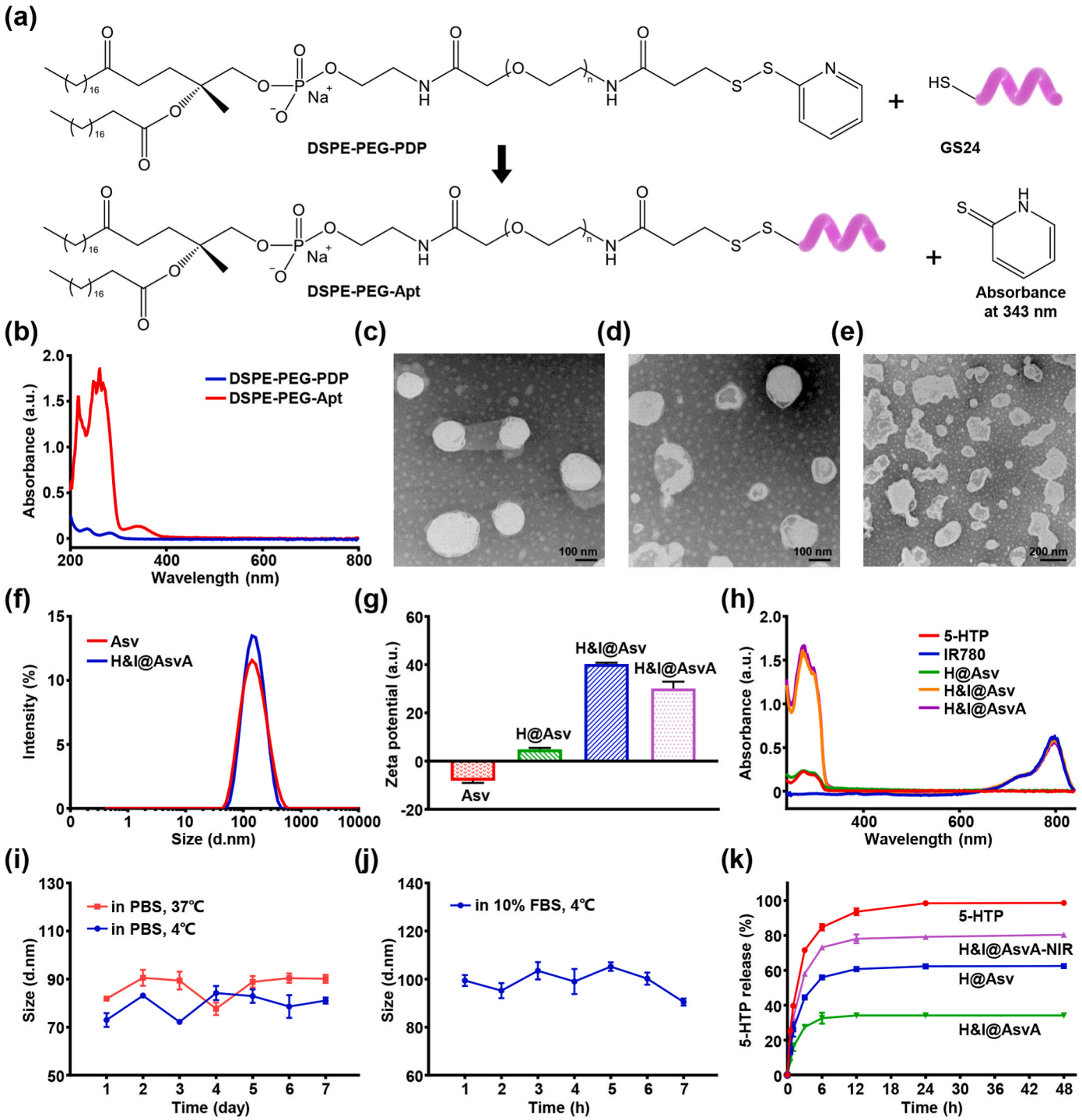

Fig. 2. Characterizations of H&I@AsvA. a) Schematic illustration of GS24 and DSPE-PEG-PDP coupling. b) UV–Vis–NIR spectra of DSPE-PEG-PDP and DSPE-PEG-Apt. c) TEM image of Asv, scale bar = 100 nm. d) TEM image of H&I@AsvA, scale bar = 100 nm. e) TEM image of ruptured H&I@AsvA after photothermal effect, scale bar = 200 nm. f) DLS analysis of the size distributions of Asv and H&I@AsvA. g) DLS analysis of the surface Zeta potential of Asv, H@Asv, H&I@Asv, and H&I@AsvA. h) UV–Vis–NIR spectra of 5-HTP, IR780, H@Asv, H&I@Asv, and H&I@AsvA. i) The 7-day stability test characterized by the size distributions of H&I@AsvA in PBS. j) The 7-h stability test characterized by the size distributions of H&I@AsvA in 10 % FBS. k) 5-HTP release rates from free 5-HTP, H@Asv, H&I@AsvA, and H&I@AsvA-NIR.

each group of mice. Subsequently, following an additional two-week treatment period, a behavioral test was administered, and the body weights of the mice were continuously recorded. The *in vivo* antidepressant effect of H&I@AsvA was evaluated by analyzing the behavioral tests of mice.

2.12. Western blot

Mouse hippocampal tissue was lysed using RIPA lysis buffer, and the supernatant obtained from centrifugation at 14 000×*g* for 10 min included proteins that required quantification. A bicinchoninic acid (BCA) kit was used to measure the total protein content. The proteins were separated using SDS-PAGE in equal quantities, thereafter,

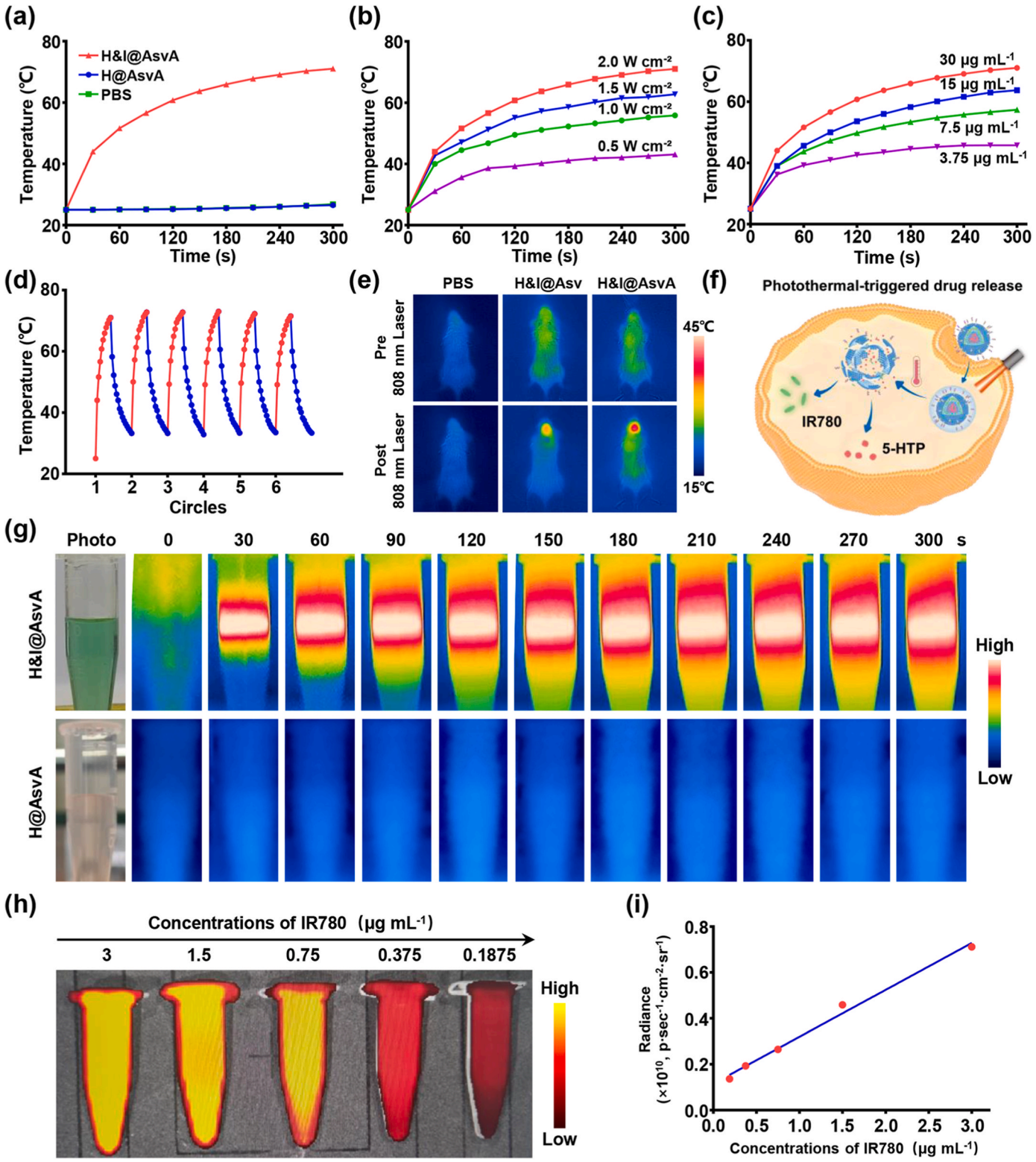

Fig. 3. *In vitro* photothermal conversion and fluorescence imaging of H&I@AsvA. a) Effect of 808 nm laser irradiation on the temperature increase of PBS, H@AsvA, and H&I@AsvA. b) Effect of 808 nm laser irradiation on the temperature increase of H&I@AsvA at 0.5, 1.0, 1.5, and 2.0 W cm^{-2}. c) Effect of 808 nm laser irradiation on the temperature increase of H&I@AsvA at concentrations of 3.750, 7.500, 15.00, and 30.00 μg mL^{-1}. d) Heating cycles of H&I@AsvA using an 808 nm laser. e) NIR thermal images of mice after being treated with PBS, H&I@Asv, and H&I@AsvA under pre- and post-irradiation conditions using an 808 nm laser. f) Schematic illustration of the photothermal effect triggering drug release. g) NIR thermal images of H@AsvA and H&I@AsvA during the photothermal conversion process. h) Fluorescence images of H&I@AsvA with different concentrations of IR780 (0.1875, 0.3750, 0.7500, 1.500, and 3.000 μg mL^{-1}). i) Linear regression of the concentrations of IR780 and fluorescence imaging intensities.

deposited onto a PVDF membrane, blocked, and incubated overnight with the primary antibody (1:2000) at 4 °C. Subsequently, the samples were washed, subjected to a 1-h incubation with the secondary antibody (1:10 000), and rinsed 6 times, each time for a duration of 5 min. The target proteins were ultimately identified using an enhanced chemiluminescence (ECL) detection reagent.

2.13. Tissue section staining

The heart, liver, spleen, lung, kidney, and brain tissues of the mice were embedded in paraffin blocks after treatment. These sections were sectioned at a thickness of 5 μm using a microtome, and then stained for microscopic examination using hematoxylin and eosin (H&E) staining, and photos were obtained. The antigen-repaired slices of the mouse brain tissues were subjected to incubation with the primary antibody, specifically the mouse monoclonal antibody at a dilution of 1:200. Subsequently, the antibody was conjugated to brain-derived neurotrophic factor (BDNF) to facilitate immunohistochemistry (IHC) labeling. A positive result was shown by the generation of a brown insoluble DAB (3,3′-diaminobenzidine) precipitate after the sections were incubated with the secondary antibody and horseradish peroxidase, and images were obtained.

2.14. Statistical analysis

The data were represented at least three times as mean ± SD. Two or more groups were compared using one-way ANOVA. No significant difference was indicated as (*n. s.*), $P < 0.05$ (*), $P < 0.01$ (**), and $P < 0.001$ (***).

3. Results and discussion

3.1. Synthesis and characterization of H&I@AsvA

In a neuron, natural synaptic vesicles contain various neurotransmitters which are released at the synapse. Synaptic vesicles have a sphere of 40 nm diameter with a lipid composition including phosphatidylcholine, phosphatidylethanolamine, phosphatidylserine, phosphatidylinositol, and cholesterol, and their surface contain two types of proteins: transport proteins that involved in the uptake of neurotransmitter, and trafficking proteins that involved in exocytosis, endocytosis, and recycling [28]. Artificial synaptic vesicles can be modified with targeted ligands including proteins to enhance specific targeting to certain tissues or cells, and they can be designed to release drugs in response to external stimuli [29]. Fig. 2a displays the DNA aptamer GS24 coupling reaction with DSPE-PEG-PDP, as stated in Table S1. Because the disulfide bond between DSPE-PEG and PDP was disrupted by the introduction of the sulfhydryl-modified DNA aptamer, a UV–Vis peak at 343 nm was observed. There was a substitution process between DSPE-PEG-PDP and the DNA aptamer GS24, as Fig. 2b shows that DSPE-PEG-Apt exhibited a strong absorbance peak at 343 nm. To create H&I@AsvA, further manufacturing steps included mixing DSPE-PEG-Apt with Asv.

Fig. 2c and d shows the TEM images of Asv and H&I@AsvA. The particles in both samples are uniformly spherical and have a size distribution of approximately 100 nm. To verify that H&I@AsvA can achieve photothermal-triggered drug release, H&I@AsvA was exposed to 808 nm laser irradiation for 5 min. The hydrated particle size of H&I@AsvA increased significantly and exhibited clear rupture, which contributed to rapid drug release in the brain (Figs. S1 and 2e). The hydrated particle size distributions of Asv and H&I@AsvA were 110.6 ± 0.6 nm and 104.2 ± 1.1 nm, respectively, as shown in Fig. 2f. The negatively charged Zeta potential of Asv was - 8.1 ± 0.9 mV, shown in Fig. 2g, whereas the positively charged Zeta potential of H@Asv was +4.9 ± 0.6 mV. The inclusion of positively charged IR780 caused H&I@Asv to have a Zeta potential of +40.3 ± 0.6 mV. Moreover, since the DNA backbone is negatively charged, the Zeta potential of H&I@AsvA somewhat decreased to +30.17 ± 2.78 mV. These results indicate that H&I@AsvA was successfully synthesized. The UV–Vis–NIR spectra of 5-HTP, IR780, H@Asv, H&I@Asv, and H&I@AsvA are shown in Fig. 2h. IR780 had a unique absorbance peak at 790 nm, while 5-HTP exhibited two distinctive peaks at 276 and 343 nm. Asv encapsulation of IR780 and 5-HTP was confirmed by the fact that H&I@Asv and H&I@AsvA had similar absorbance peaks to those of IR780 and 5-HTP, respectively. At either 4 or 37 °C, the solution remained clear and transparent in PBS, and there was no discernible change in the hydrated particle size within 7 days (Fig. 2i and j). On the other hand, after 7 h in 10 % FBS at 4 °C, the hydrated particle size hardly changed, and the solution maintained its clarity and transparency. These findings show that H&I@AsvA has excellent *in vitro* stability.

3.2. The controlled release of 5-HTP from H&I@AsvA

Figs. S2a and S2b show the UV–Vis spectra of 5-HTP standard curves and various 5-HTP concentrations. The DLC and DEE of 5-HTP were determined to be 15.5 % and 55.6 %, respectively. The *in vitro* drug release curves of free 5-HTP, H@Asv, H&I@AsvA, and H&I@AsvA after 808 nm laser irradiation are shown in Fig. 2k. With a release rate of more than 90 % after 12 h and 70 % after 3 h, free 5-HTP exhibited the fastest drug release rate. Asv encapsulation successfully regulated 5-HTP release, as H@Asv was able to decrease the release rate by 62.5 % after 48 h. The encapsulation of IR780 within the liposomal phospholipid bilayers made Asv more rigid and may have contributed to the extension of the half-life of 5-HTP *in vivo*, and the release of 5-HTP was only 34.2 % after 48 h, in comparison to that of free 5-HTP and H@Asv. Furthermore, the incorporation of IR780 allowed H&I@AsvA to achieve photothermal-triggered drug release, resulting in the regulated rapid release of 5-HTP in the brain. Moreover, to verify the photothermal-triggered drug release performance of H&I@AsvA, H&I@AsvA was irradiated with an 808 nm laser at 2.0 W cm^{-2} for 5 min before dialysis. Compared to that of the H&I@AsvA group, the 5-HTP release rate of the H&I@AsvA group was significantly greater than that of the H&I@AsvA-NIR group, which was attributed to the rupture of Asv caused by photothermal heat, resulting in the rapid release of 5-HTP (Figs. S1 and 2e).

3.3. In vitro photothermal effects of H&I@AsvA

Under 808 nm laser irradiation at 2.0 W cm^{-2}, the photothermal curves of PBS, H@AsvA, and H&I@AsvA are shown in Fig. 3a. The temperatures of PBS, H@AsvA, and H&I@AsvA were elevated to 26.5, 26.8, and 71.0 °C, respectively. Fig. 3b displays the photothermal curves of H&I@AsvA (IR780 concentration: 30 μg mL^{-1}) when exposed to varying powers of laser light, and Fig. 3c shows H&I@AsvA exposed to an 808 nm laser at 2.0 W cm^{-2} with varying IR780 concentrations. Based on the temperature-changed curves after 808 nm laser irradiation (Fig. 3d), H&I@AsvA demonstrated excellent photothermal stability even after repeated heating, and its PCE was determined to be 49.01 %. Fig. 3e also displays the results of the *in vivo* photothermal performance investigation. The temperature of the PBS group rose from 27.2 to 27.4 °C before irradiation and after 5 min of 808 nm laser irradiation; the temperature of the H&I@Asv group rose from 29.3 to 37.6 °C, and the temperature of the H&I@AsvA group rose from 28.8 to 43.7 °C. These findings indicate that H&I@AsvA can achieve effective photothermal conversion in the brain. Fig. 3f shows the design of the H&I@AsvA drug release system, which is driven by photothermal power, and Fig. 3g shows NIR thermal images of the photothermal conversion process. Together, these investigations demonstrate the exceptional photothermal performance of H&I@AsvA.

3.4. In vitro fluorescence imaging of H&I@AsvA

The fluorescence intensity of H&I@AsvA was positively correlated

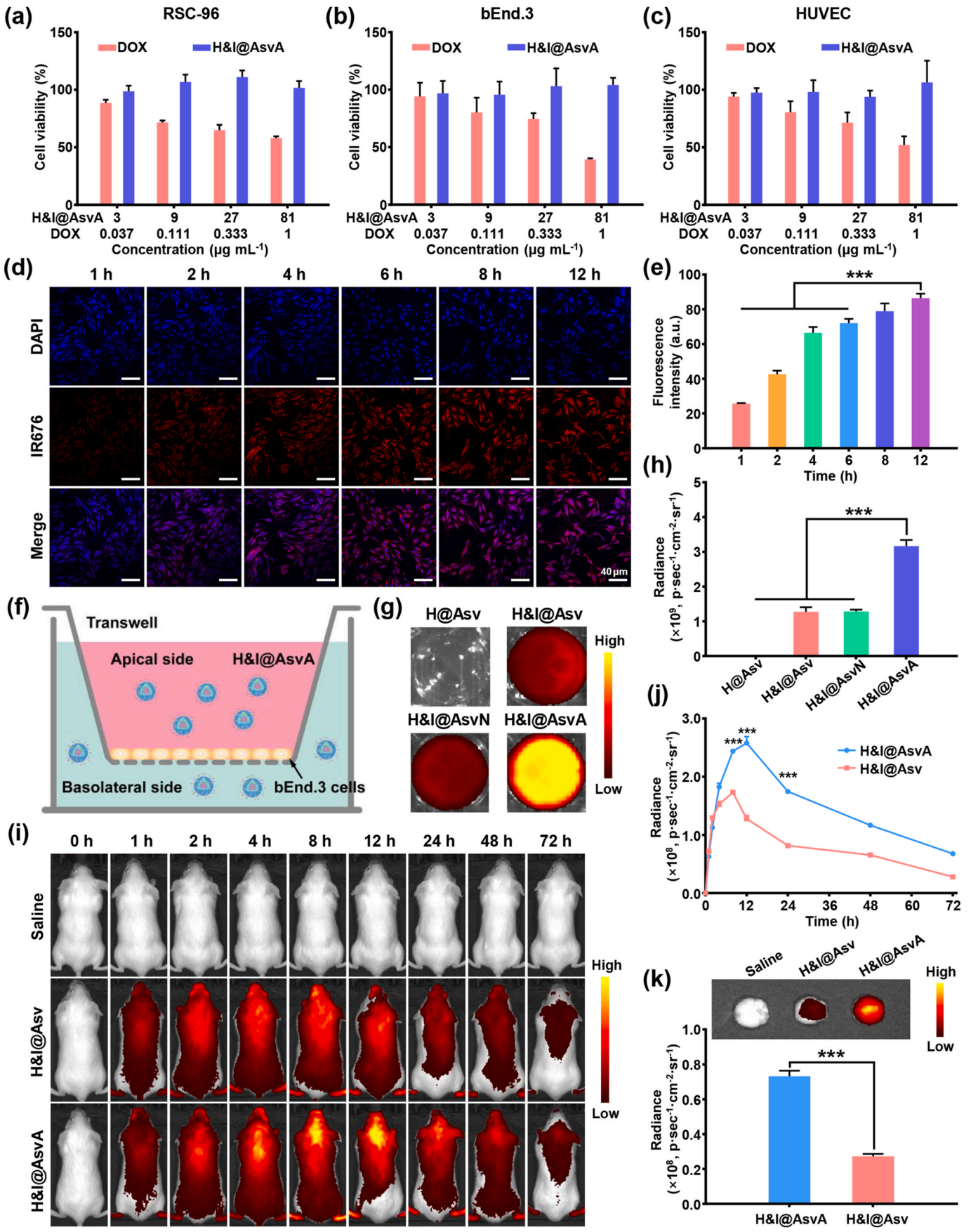

(caption on next page)

Fig. 4. *In vitro* cell culture studies and *in vivo* fluorescence imaging. a) Cell viability of RSC-96 cells after incubation with H&I@AsvA and DOX. b) Cell viability of bEnd.3 cells after incubation with H&I@AsvA and DOX. c) Cell viability of HUVECs after incubation with H&I@AsvA and DOX. d) Fluorescence images of the cell internalization of H&I@AsvA (IR780 was replaced with IR676) at 1, 2, 4, 6, 8, and 12 h, scale bars = 40 μm. e) Quantitative fluorescence imaging data of cell internalization of H&I@AsvA at 1, 2, 4, 6, 8, and 12 h. f) Schematic illustration of the *in vitro* BBB model. g) Fluorescence images of the basolateral side of the Transwell plate supplemented with H@Asv, H&I@Asv, H&I@AsvN, and H&I@AsvA. h) Fluorescence imaging quantitative data of the basolateral side of the Transwell plate. i) *In vivo* fluorescence imaging of H&I@AsvA targeting brain areas of mice at 0, 1, 2, 4, 8, 12, 24, 48, and 72 h. j) Fluorescence imaging quantitative data of brain areas at 0, 1, 2, 4, 8, 12, 24, 48, and 72 h. k) *Ex vivo* fluorescence imaging of brains.

with the concentration of IR780, showing that the greater IR780 concentration led to brighter fluorescence of the H&I@AsvA within a particular concentration range (Fig. 3h and i).

3.5. In vitro cell culture studies of H&I@AsvA

Both H&I@AsvA and DOX (the positive control) were tested for cell viability using the CCK-8 assay. The cell viability of RSC-96 cells, bEnd.3 cells, and HUVECs are shown in Fig. 4a, b, and c, respectively. As the concentration of DOX increased, cell viability decreased; DOX was the most lethal to bEnd.3 cells. Nevertheless, the cell viability of all three cell lines remained consistently high as the concentration of H&I@AsvA increased; eventually, the cell viability reached almost 100 %, suggesting that the Asv used as nanocarriers were nearly free of cytotoxicity and that H&I@AsvA exhibited excellent biosafety.

CLSM images of H&I@AsvA internalization are shown in Fig. 4d. The fact that IR676 slowly accumulated in the cytoplasm suggested that H&I@AsvA was successful in delivering IR676 into the cells and achieving this accumulation. Fig. 4e shows the fluorescence quantification of cell internalization; as the incubation period increased, the quantity of IR676 in the cytoplasm considerably increased.

3.6. In vitro and in vivo active targeting of H&I@AsvA

Fig. 4f depicts a schematic of the *in vitro* BBB model. H@Asv, H&I@Asv, H&I@AsvN (N: Non-targeting sequence DNA with the same number of bases as GS24), and H&I@AsvA were added to the apical side of the Transwell plate. Fig. 4g and h shows the quantification and fluorescence images of the basolateral side after 12 h. None of the H@Asv group fluoresced, whereas the H&I@Asv and H&I@AsvN groups showed lower fluorescence intensity, suggesting that the permeability of the BBB was unaffected by non-targeting sequence DNA-modified Asv. In contrast, the H&I@AsvA group was remarkably more efficient at penetrating the BBB, and its fluorescence intensity was noticeably greater than that of the other groups (***$P < 0.001$).

We also confirmed that H&I@AsvA could penetrate the BBB *in vivo*. The fluorescence images and quantification of each mouse group *in vivo* throughout 72 h (0, 1, 2, 4, 8, 12, 24, 48, and 72 h) are shown in Fig. 4i and j, respectively. Before the injection, neither group had any fluorescence signal. After injection, the fluorescence signal in the brain area was greatest at 8 and 12 h in the H&I@Asv and H&I@AsvA groups, respectively. In terms of the enrichment rate and efficiency, H&I@AsvA outperformed H&I@Asv, and its fluorescence intensity was noticeably greater. Overall, the fluorescence signal in the brain area of H&I@AsvA was greater than that in the brain area of H&I@Asv. Fig. 4k and S3 demonstrate that the fluorescence imaging of brains and organs of mice were excised at 72 h. The fluorescence of H&I@AsvA at 72 h was significantly greater than that of H&I@Asv, and the fluorescence in the brain of mice in the H&I@Asv group nearly disappeared at 72 h. The nanoplatforms mainly accumulated in the brain, liver, lung, and kidney. The fluorescence imaging *in vitro* and *in vivo* demonstrated that aptamer-modified Asv were able to enhance their targeting and BBB crossing capabilities, leading to more efficient targeted 5-HTP release in the brain.

3.7. Hemolysis and acute toxicity testing of H&I@AsvA

The results depicted in Fig. 5a indicate that the Triton X-100 group exhibited notable hemolysis. In contrast, the Asv, H@Asv, H&I@Asv, and H&I@AsvA groups displayed minimal hemolysis, with hemolysis rates of 0.30 %, 0.84 %, 0.19 %, and 0.82 %, respectively (Fig. 5a). The behavioral activity of the mice in all the groups was normal, the survival rate was 100 %, and the body weight was within the normal range throughout the 14-day acute toxicity test (Fig. 5b and c). The potential toxicity of the nanoplatform to mice could be further verified by histopathological observation and whole blood biochemical indices. The results of H&E staining and liver, renal function, and cardiac enzyme tests are shown in Fig. 5d and e. Pathological observation revealed that the nanomaterials in each group did not cause any damage to the organs and tissues of the mice. Compared with the control group (saline group), nanoplatform-treated mice showed no significant changes in biochemical indices. Specifically, liver function indices such as alanine transaminase (ALT), aspartate aminotransferase (AST), γ-glutamyl transferase (γ-GT), total bilirubin (T-BIL), and direct bilirubin (D-BIL), renal function indices such as creatinine (CREA), UREA, and blood urea nitrogen (BUN), as well as cardiac enzyme indices such as lactate dehydrogenase (LDH), lactate dehydrogenase isozyme 1 (LDH1), creatine kinase (CK), and creatine kinase isoenzymes (CK-MB) were within the reference range. The above results indicate that the nanomaterials in each group have a high level of animal safety.

3.8. In vivo antidepressant treatment

A schematic representation of the method used to assess antidepressant therapy efficacy is shown in Fig. 6a. The CUMS mouse model, which was constructed as described in Table S2, had a much lower weight before treatment (Fig. 6b). After 2 weeks of treatment, the mice in the H&I@AsvA and H&I@AsvA-NIR groups progressively recovered and returned to normal body weights after 4 weeks of treatment, whereas the other groups only exhibited a modest increase in body weight after 4 weeks of treatment.

Fig. 6c shows the results of the SPT. Before treatment, the control group mice had a strong preference for sucrose (over 90 %), whereas the CUMS model mice, who were given either regular water or sugar water at random, preferred sucrose of approximately 50 %. Some relief from depressive-like behavior was shown by an increase in the sucrose preference to over 80 % in the H&I@AsvA-NIR group mice and approximately 60 % in the H&I@AsvA group mice after 2 weeks of therapy. Mice in the H&I@AsvA and H&I@AsvA-NIR groups showed a sucrose preference that was similar to that of the control group after 4 weeks of therapy, and the sucrose preference in the saline, 5-HTP, and H&I@Asv groups of mice remained low.

Fig. 6d displays the results of the FST. Before the treatment, the mice in the control group were constantly moving, with an immobility duration of approximately 100 s. In contrast, the CUMS mice remained motionless for more than 160 s in almost all of them, and for some of them, the immobility duration was more than 200 s. The mice in the H&I@AsvA-NIR group exhibited a significant improvement in their depression-like behaviors and a reduction in their immobility time to approximately 100 s after 2 weeks of therapy. At the same time, the mice in the H&I@AsvA group exhibited only a slight alleviation of depressive-like behaviors. After 4 weeks of treatment, the mice returned to normal. The mice treated with H&I@Asv for 4 weeks demonstrated a modest improvement in depressive behaviors and an alleviation in immobility time to approximately 130 s. However, the mice treated with saline or 5-HTP for 4 weeks exhibited considerable depressive-like behavior.

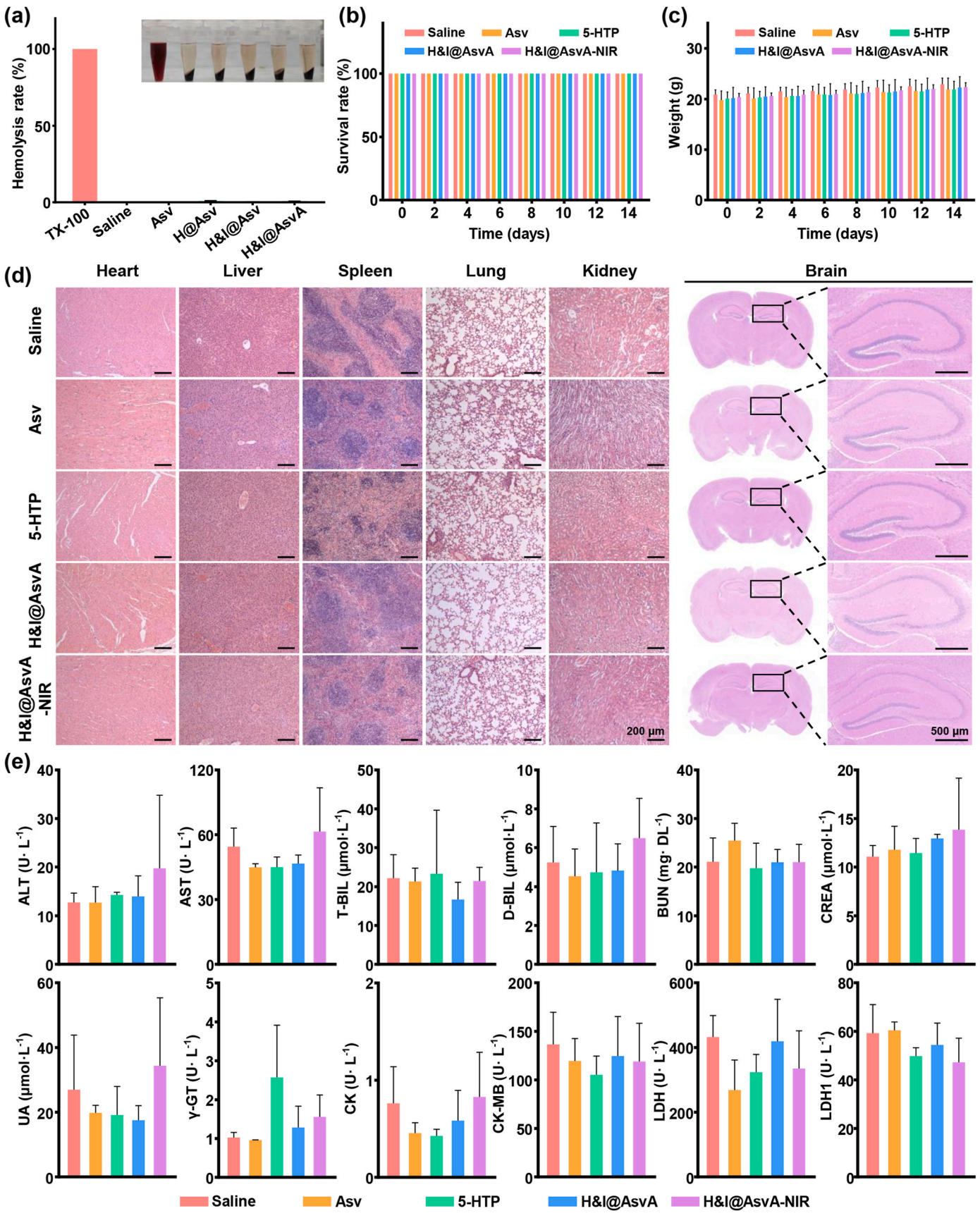

Fig. 5. Biosafety of H&I@AsvA. a) Hemolysis of Asv, H@Asv, H&I@Asv, and H&I@AsvA. Triton X-100 and saline were positive and negative controls. b) Survival rate of mice in the 14-day acute toxicity test. c) Body weight of mice in the 14-day acute toxicity test. d) H&E-stained tissues from the main organs of mice after acute toxicity test (heart, liver, spleen, lung, kidney, scale bars = 200 μm; brain, scale bars = 500 μm). e) Liver, renal function, and cardiac enzyme tests.

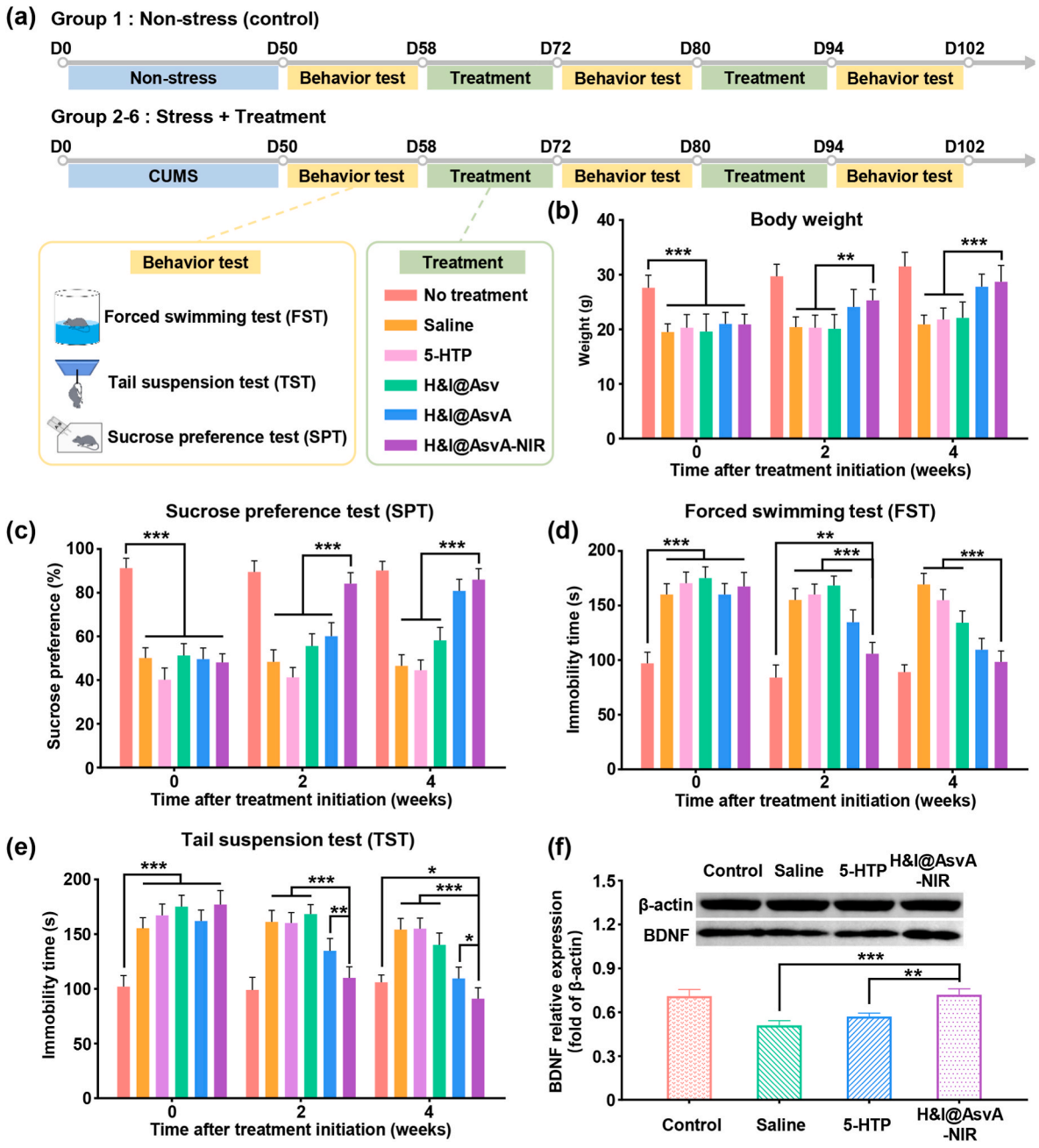

Fig. 6. *In vivo* antidepressant treatment. a) Schematic illustration of the *in vivo* antidepressant treatment. b) The body weight of each group of mice was measured every 2 weeks. c-e) Depressive-like behavior was measured by the SPT, FST, and TST. f) Representative western blot images and relative levels quantification of BDNF protein in mouse brain hippocampal tissue.

Fig. 6e displays the results of the TST. The mice in the control group had a very short immobility period of approximately 100 s before treatment. With an immobility period of more than 150 s, almost all the CUMS mice remained motionless. After 2 weeks of treatment, the mice in the H&I@AsvA-NIR group exhibited significant improvements in depressive-like behaviors. After 4 weeks of treatment, the mice completely returned to their normal states. After 2 weeks of therapy, the depressive-like behaviors of the mice in the H&I@AsvA group were only slightly alleviated, and after 4 weeks of treatment, the depressive-like behaviors of the mice returned to normal; however, the depressive-like behaviors of the mice in the H&I@Asv group were only slightly alleviated after 4 weeks of treatment. The mice treated with saline or 5-HTP for 4 weeks exhibited considerable depressive-like behavior. After 4 weeks of therapy, the statistical analysis revealed that the H&I@AsvA-NIR group differed significantly from the saline, 5-HTP, or H&I@Asv groups in terms of body weight, sucrose preference, and immobility time in the FST and TST (***$P < 0.001$).

3.9. Brain tissue analysis in hippocampus

Western blot analysis revealed that after 4 weeks of treatment, the hippocampal BDNF levels in the saline and 5-HTP groups were substantially lower than those in the control and H&I@AsvA-NIR groups (Fig. 6f). The assessment of relative BDNF levels in the hippocampus showed that BDNF levels differed significantly between the H&I@AsvA-NIR group and the saline group (***$P < 0.001$). Furthermore, we analyzed the H&E-stained sections of post-treatment mouse organs and brain tissues. Fig. 7 demonstrates that after treatment, no cell necrosis or

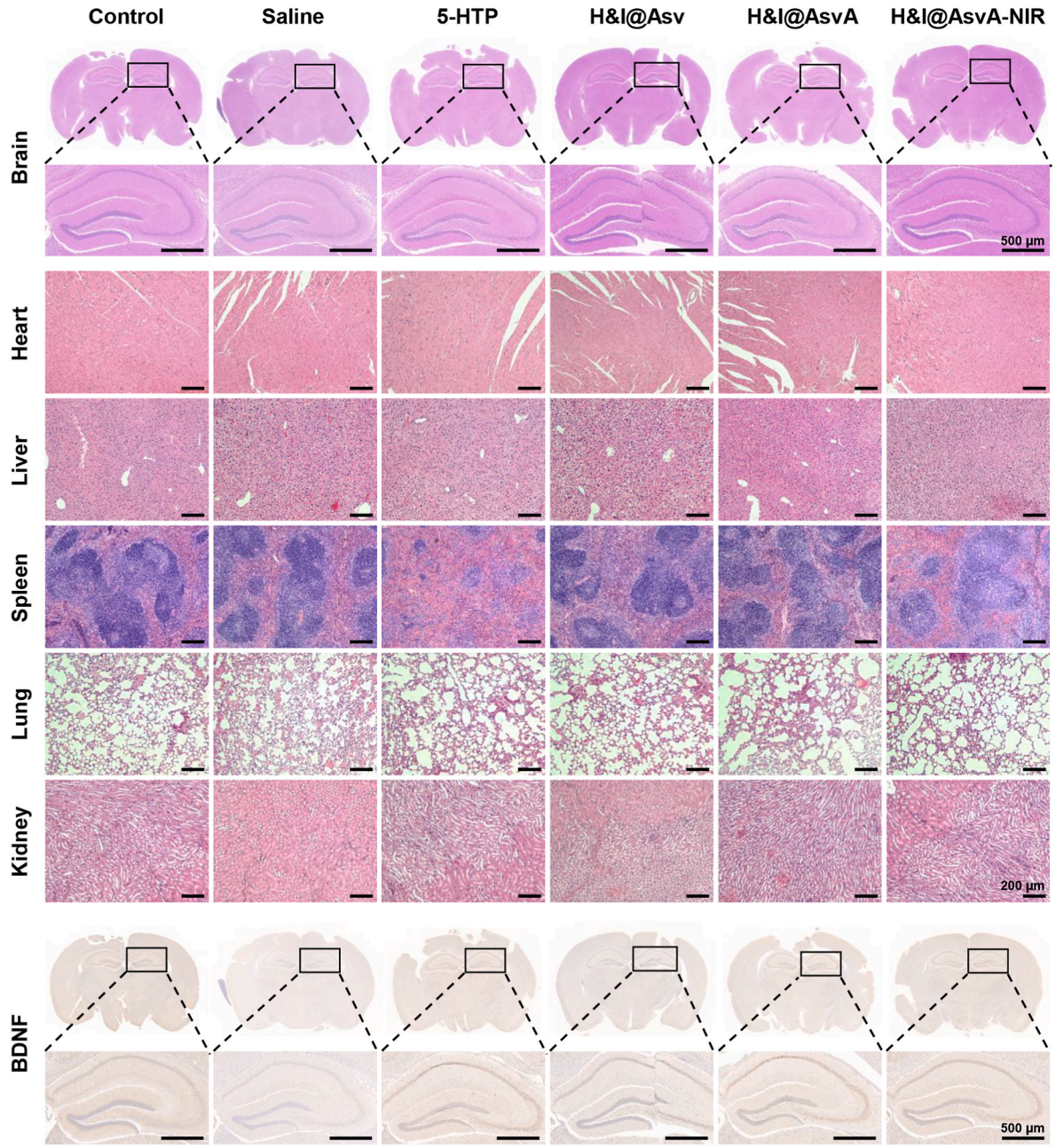

Fig. 7. H&E staining and IHC analysis of mouse brain tissue and H&E staining of the heart, liver, spleen, lung, and kidney of mice from each group (heart, liver, spleen, lung, kidney, scale bars = 200 μm; brain, scale bars = 500 μm).

tissue damage was observed in the heart, liver, spleen, lung, kidney, and brain of the mice in any group. This finding points to the high biosafety of H&I@AsvA and mild photothermal therapy.

As demonstrated in Fig. 7, BDNF was analyzed in mouse brain tissue using IHC analysis. The BDNF expression in the saline group was significantly lower than that in the control group, and the BDNF levels in the 5-HTP, H&I@Asv, H&I@AsvA, and H&I@AsvA-NIR groups were elevated to different degrees. The results of the IHC analysis differed slightly from those of the behavioral tests, possibly because the improvement of depression-like behaviors in mice occurs after BDNF levels increase, suggesting that conventional drug delivery methods have a slow effect, in contrast to H&I@AsvA combined with mild photothermal therapy, which can alleviate depressive-like behaviors rapidly, resulting in rapid-acting treatment for depression.

Fig. 8 displays the entire procedure, from the development of the CUMS mouse model to the end of the 4-week treatment, and the depression-like levels of each group of mice at various time points are shown.

4. Conclusions

In conclusion, we created a NIR light-responsive H&I@AsvA nanoplatform loaded with 5-HTP and IR780 and functionalized it with an aptamer for efficient targeting and crossing of the BBB. The biosafety and minimal cytotoxicity of H&I@AsvA were shown in both *in vitro* and *in vivo* studies. Moreover, an *in vitro* BBB model and *in vivo* fluorescence imaging verified that H&I@AsvA can effectively cross the BBB, resulting in photothermal-triggered 5-HTP release in the brain and improving the rate and efficiency of 5-HTP accumulation. In CUMS mice, H&I@AsvA in combination with mild photothermal therapy considerably reduced depressive-like behaviors within 2 weeks and alleviated them completely within 4 weeks, according to *in vivo* antidepressant

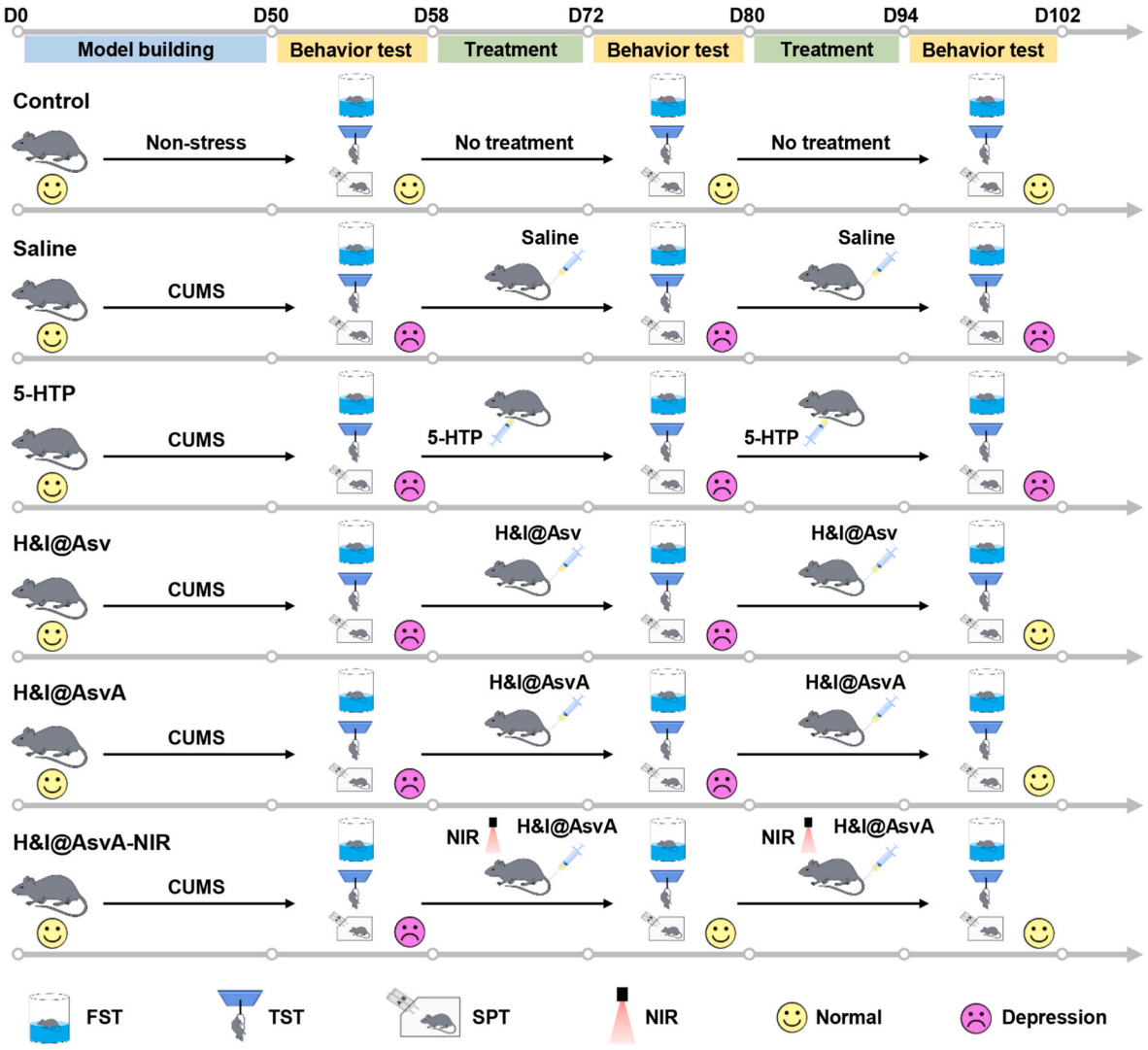

Fig. 8. Schematic representation of the effect of antidepressant treatment *in vivo*. The mice were divided into six groups: control, saline (intravenous saline), 5-HTP (intraperitoneal injection of 5-HTP), H&I@Asv (intravenous H&I@Asv), H&I@AsvA (intravenous H&I@AsvA), and H&I@AsvA-NIR (intravenous H&I@AsvA with 808 nm laser irradiation).

treatment behavioral tests, IHC analysis, and western blotting. The nanoplatform has greatly shortened the duration of depression therapy and shows potential for use in clinical treatments in the future.

CRediT authorship contribution statement

Peng Chang: Writing – original draft, Visualization, Methodology, Investigation, Formal analysis, Data curation, Conceptualization. **Jingwen Ma:** Funding acquisition, Data curation. **Ke Li:** Resources, Funding acquisition. **Wei Wang:** Funding acquisition, Data curation. **Dan Chen:** Validation. **Zhe Liu:** Data curation. **Wenhua Zhan:** Writing – review & editing, Supervision, Project administration, Funding acquisition. **Yun Zeng:** Writing – review & editing, Project administration, Funding acquisition, Conceptualization. **Yonghua Zhan:** Writing – review & editing, Supervision, Project administration, Funding acquisition.

Declaration of competing interest

The authors declare that they have no known competing financial interests or personal relationships that could have appeared to influence the work reported in this paper.

Acknowledgements

This work was supported, in part, by the National Natural Science Foundation of China (Nos. 32001074, 82260473), the Key Research and Development Program in Ningxia Province of China (No. 2023BEG03035), the Natural Science Basic Research Key Program of Shaanxi Province (Nos. 2023-JC-ZD-53, 2024JC-ZDXM-47), the Natural Science Basic Research Key Program of Ningxia Province of China (No. 2024AAC02079), the Fundamental Research Funds for the Central Universities (Nos. ZYTS24149, xzy012022134), and the Xidian University Specially Funded Project for Interdisciplinary Exploration (Nos. TZJH2024029, TZJH2024030).

Appendix A. Supplementary data

Supplementary data to this article can be found online at https://doi.org/10.1016/j.mtbio.2024.101357.

Data availability

Data will be made available on request.

References

[1] S. Marwaha, E. Palmer, T. Suppes, E. Cons, A.H. Young, R. Upthegrove, Novel and emerging treatments for major depression, Lancet 401 (2023) 141–153.

[2] H. Herrman, C. Kieling, P. McGorry, R. Horton, J. Sargent, V. Patel, Reducing the global burden of depression: a lancet-world psychiatric association commission, Lancet 393 (2019) e42–e43.

[3] S.E. Murphy, L.P. Capitão, S.L. Giles, P.J. Cowen, A. Stringaris, C.J. Harmer, The knowns and unknowns of SSRI treatment in young people with depression and anxiety: efficacy, predictors, and mechanisms of action, Lancet Psychiatry 8 (2021) 824–835.

[4] D.J. Nutt, Relationship of neurotransmitters to the symptoms of major depressive disorder, J. Clin. Psychiatry 69 (2008) 4–7.

[5] F.C. Gabriel, D.O. de Melo, R. Fráguas, N.C. Leite-Santos, R.A. Mantovani da Silva, E. Ribeiro, Pharmacological treatment of depression: a systematic review comparing clinical practice guideline recommendations, PLoS One 15 (2020) e0231700.

[6] T. Kendrick, S. Collinson, Antidepressants and the serotonin hypothesis of depression, Br. Med. J. 378 (2022) o1993.

[7] N. Sun, Y. Qin, C. Xu, T. Xia, Z. Du, P. Zheng, A. Li, F. Meng, Y. Zhang, J. Zhang, X. Liu, Design of fast-onset antidepressant by dissociating SERT from nNOS in the DRN, Science 378 (2022) 390–398.

[8] X. Zhou, C. Zhao, H. Xu, Y. Xu, L. Zhan, P. Wang, J. He, T. Lu, Y. Gu, Y. Yang, C. Xu, Pharmacological inhibition of Kir4.1 evokes rapid-onset antidepressant responses, Nat. Chem. Biol. 20 (2024) 857–866.

[9] M.H. Trivedi, A.J. Rush, S.R. Wisniewski, A.A. Nierenberg, D. Warden, L. Ritz, G. Norquist, R.H. Howland, B. Lebowitz, P.J. McGrath, K. Shores-Wilson, Evaluation of outcomes with citalopram for depression using measurement-based care in STAR*D: implications for clinical practice, Am. J. Psychiatry 163 (2006) 28–40.

[10] N. Iovieno, E.D. Dalton, M. Fava, D. Mischoulon, Second-tier natural antidepressants: review and critique, J. Affective Disord. 130 (2011) 343–357.

[11] S. Fu, H. Chen, W. Yang, X. Xia, S. Zhao, X. Xu, P. Ai, Q. Cai, X. Li, Y. Wang, J. Zhu, ROS-targeted depression therapy via BSA-incubated ceria nanoclusters, Nano Lett. 22 (2022) 4519–4527.

[12] J.P. Jacobsen, A.D. Krystal, K.R.R. Krishnan, M.G. Caron, Adjunctive 5-Hydroxy-tryptophan slow-release for treatment-resistant depression: clinical and preclinical rationale, Trends Pharmacol. Sci. 37 (2016) 933–944.

[13] J.P. Jacobsen, A. Oh, R. Bangle, W.L. Roberts, E.L. Royer, N. Modesto, S. A. Windermere, Z. Yi, R. Vernon, M. Cajina, N.M. Urs, Slow-release delivery enhances the pharmacological properties of oral 5-hydroxytryptophan: mouse proof-of-concept, Neuropsychopharmacology 44 (2019) 2082–2090.

[14] L. Jin, P. Hu, Y. Wang, L. Wu, K. Qin, H. Cheng, S. Wang, B. Pan, H. Xin, W. Zhang, X. Wang, Fast-acting black-phosphorus-assisted depression therapy with low toxicity, Adv. Mater. 32 (2020) 1906050.

[15] C. Ferraris, R. Cavalli, P.P. Panciani, L. Battaglia, Overcoming the blood-brain barrier: successes and challenges in developing nanoparticle-mediated drug delivery systems for the treatment of brain tumours, Int. J. Nanomedicine 15 (2020) 2999–3022.

[16] S. Zha, H. Liu, H. Li, H. Li, K.L. Wong, A.H. All, Functionalized nanomaterials capable of crossing the blood-brain barrier, ACS Nano 18 (2024) 1820–1845.

[17] J. Wang, J. Xu, G. Zang, T. Zhang, Q. Wu, H. Zhang, Y. Chen, Y. Wang, W. Qin, S. Zhao, E. Qin, J. Qiu, X. Zhang, L. Wen, Y. Wang, G. Wang, Trans-2-enoyl-CoA reductase Tecr-driven lipid metabolism in endothelial cells protects against transcytosis to maintain blood-brain barrier homeostasis, Research 2022 (2022) 9839368.

[18] N. Palani, P. Vijayakumar, P. Monisha, S. Ayyadurai, S. Rajadesingu, Electrospun nanofibers synthesized from polymers incorporated with bioactive compounds for wound healing, J. Nanobiotechnology 22 (2024) 603.

[19] W. Zhang, H. Chen, L. Ding, J. Huang, M. Zhang, Y. Liu, R. Ma, S. Zheng, J. Gong, J. C. Piña-Crespo, Y. Zhang, Microglial targeted therapy relieves cognitive impairment caused by Cntnap4 deficiency, Exploration 3 (2023) 20220160.

[20] C. Hernandez, S. Shukla, Liposome based drug delivery as a potential treatment option for Alzheimer's disease,, Neural Regeneration Research 17 (2022) 1190–1198.

[21] A.J. Pickering, N.G. Lamson, M.H. Marand, W. Hwang, J.P. Straehla, P. T. Hammond, Layer-by-layer polymer functionalization improves nanoparticle penetration and glioblastoma targeting in the brain, ACS Nano 17 (2023) 24154–24169.

[22] M. Sela, M. Poley, P. Mora-Raimundo, S. Kagan, A. Avital, M. Kaduri, G. Chen, O. Adir, A. Rozencweig, Y. Weiss, O. Sade, Y. Leichtmann-Bardoogo, L. Simchi, S. Aga-Mizrachi, B. Bell, Y. Yeretz-Peretz, A.Z. Or, A. Choudhary, I. Rosh, D. Cordeiro, S. Cohen-Adiv, Y. Berdichevsky, A. Odeh, J. Shklover, J. Shainsky-Roitman, J.E. Schroeder, D. Hershkovitz, P. Hasson, A. Ashkenazi, S. Stern, T. Laviv, A. Ben-Zvi, A. Avital, U. Ashery, B.M. Maoz, A. Schroeder, Brain-targeted liposomes loaded with monoclonal antibodies reduce alpha-synuclein aggregation and improve behavioral symptoms in Parkinson's disease, Adv. Mater. 35 (2023) 2304654.

[23] Y. Zhang, J. He, L. Shen, T. Wang, J. Yang, Y. Li, Y. Wang, D. Quan, Brain-targeted delivery of obidoxime, using aptamer-modified liposomes, for detoxification of organophosphorus compounds, J. Controlled Release 329 (2021) 1117–1128.

[24] T. Li, Y. Liu, W. Bao, J. Luo, L. Gao, X. Chen, S. Wang, J. Yu, Y. Ge, B. Zhang, N. Xie, Z. Xie, T. Chen, H. Zhang, Synergistic photothermal and chemical therapy by smart dual-functional graphdiyne nanosheets for treatment of Parkinson's Disease, Adv. Ther. 4 (2021) 2100082.

[25] Y. Zeng, L. Zhao, K. Li, J. Ma, D. Chen, C. Liu, W. Zhan, Y. Zhan, Aptamer-functionalized nanoplatforms overcoming temozolomide resistance in synergistic chemo/photothermal therapy through alleviating tumor hypoxia, Nano Res. 16 (2023) 9859–9872.

[26] Y. Zhang, C. Zhang, J. Liu, H. Shao, Alzheimer's disease: potential pathogenesis and imaging findings, View 4 (2023) 20230025.

[27] K. Sou, D.L. Le, H. Sato, Nanocapsules for programmed neurotransmitter release: toward artificial extracellular synaptic vesicles, Small 15 (2019) 1900132.

[28] T.C. Südhof, The synaptic vesicle cycle, Annu. Rev. Neurosci. 27 (2004) 509–547.

[29] T.C. Südhof, The synaptic vesicle cycle: a cascade of protein-protein interactions, Nature 375 (1995) 645–653.